

## CONFIRMING THE DETECTION OF AN INTERGALACTIC X-RAY ABSORBER TOWARD PKS 2155-304

TAOTAO FANG<sup>1</sup>, CLAUDE R. CANIZARES<sup>2</sup>, YANGSEN YAO<sup>2</sup>

*Draft version February 1, 2008*

### ABSTRACT

We present new observations on PKS 2155-304 with the *Chandra* Low Energy Transmission Grating Spectrometer (LETG), using the Advanced CCD Imaging Spectrometer (ACIS). We confirm the detection of an absorption line plausibly identified as O VIII Ly $\alpha$  from the warm-hot intergalactic medium associated with a small group of galaxies along the line of sight, as originally reported by Fang et al. 2002 (here after FANG02). Combining the previous observations in FANG02 and five new, long observations on the same target, we increase the total exposure time by a factor of three, and the total counts per resolution element by a factor of five. The measured line equivalent width is smaller than that observed in FANG02, but still consistent at 90% confidence. We also analyze the *XMM*-Newton observations on the same target, as well as observations using the *Chandra* LETG and the High Resolution Camera (HRC) combination. These observations have been used to challenge our reported detection. While no line is seen in either the *XMM*-Newton and the *Chandra* LETG+HRC data, we find that our result is consistent with the upper limits from both data sets. We attribute the non-detection to (1) higher quality of the *Chandra* LETG+ACIS spectrum, and (2) the rather extended wings of the line spread functions of both the *XMM* RGS and the *Chandra* LETG+HRC. We discuss the implication of our observation on the temperature and density of the absorber. We also confirm the detection of  $z \sim 0$  O VII absorption and, comparing with previous *Chandra* analysis, we obtain much tighter constraints on the line properties.

*Subject headings:* intergalactic medium — quasars: absorption lines — X-rays: galaxies — large-scale structure of universe — methods: data analysis

### 1. INTRODUCTION

Cosmological hydrodynamic simulations predict that a large amount of baryons in the local universe reside in the intergalactic medium (IGM) (see, e.g., Cen & Ostriker 1999; Dave et al. 2001; Kravtsov et al. 2002; Cen & Ostriker 2006). While the warm and photo-ionized Ly $\alpha$  clouds contain a significant fraction of the total baryons (see, e.g., Morris et al. 1991; Bahcall et al. 1991; Stocke et al. 1995; Shull et al. 1996; Penton et al. 2000; Williger et al. 2006; Lehner et al. 2007), the remainder is shock-heated to temperatures between  $10^5 - 10^7$  K with moderate overdensities. Highly ionized metals in this Warm-Hot Intergalactic Medium, or “WHIM”, can produce detectable absorption signatures in the UV/X-ray spectra of background sources, just as the cooler IGM imprints the Ly $\alpha$  forest (see, e.g., Perna & Loeb 1998; Hellsten 1998; Fang, Bryan, & Canizares 2002; Chen et al. 2002; Viel et al. 2003; Fujimoto et al. 2004; Furlanetto et al. 2005; Cen & Fang 2006; Kawahara et al. 2006). Detectability of the WHIM gas through emission is also under investigation (see, e.g., Croft et al. 2001; Phillips et al. 2001; Kuntz & Snowden et al. 2001; Zappacosta et al. 2002, 2005, 2007; Yoshikawa et al. 2003, 2004; Kaastra 2004; Mitza et al. 2004; Slotan et al. 2005; Fang et al. 2005; Ursino & Galeazzi 2006; Cen & Fang 2006; Takei et al. 2007a, 2007b; Mannucci et al. 2007).

Recent detections of the UV absorption lines with the STIS onboard the *Hubble* Space Telescope and the Far Ultraviolet Spectrometer (*FUSE*) have firmly revealed the existence of the WHIM gas at temperatures between  $10^5 - 10^{5.5}$  K (see, e.g., Savage et al. 1998; Tripp et al. 2000; Oegerle et al. 2000;

Sembach et al. 2004; Tumlinson et al. 2005; Danforth & Shull 2005; Stocke et al. 2006). The O VI doublet at 1032 and 1039 Å can be used to probe the temperatures, densities and redshifts of that component of the intervening WHIM gas. Recently, a population of intervening broad HI Ly $\alpha$  absorbers (BLAs) have also been detected in the far-UV band, stirring interests in probing WHIM with BLAs (see, e.g., Richter et al. 2005; 2006). The contribution of both BLAs and O VI absorbers to the baryonic density are  $\Omega_b(\text{BLA}) \geq 0.0027$  (Richter et al. 2005) and  $\Omega_b(\text{OVI}) \sim 0.0022$  (see, e.g., Danforth & Shull 2005), respectively, assuming a Hubble constant of  $70 \text{ km s}^{-1} \text{Mpc}^{-1}$ . However, as simulations suggest, about only one third of the WHIM gas can be detected in the UV band — with higher temperatures the remaining two thirds can only be revealed in the X-ray (see, e.g., Fang, Bryan, & Canizares 2002; Chen et al. 2002; Viel et al. 2003; Cen & Fang 2006; Cen & Ostriker 2006).

Several lines of evidence indicate that the narrow X-ray absorption lines from the WHIM gas may be detected with high resolution spectrometers onboard *Chandra* and *XMM*-Newton. A number of  $z \approx 0$  absorption lines were detected in the spectra of background AGNs with *Chandra* and *XMM*-Newton (Nicastro et al. 2002; Fang, Sembach, & Canizares 2003; Rasmussen et al. 2003; Kaspi et al. 2002; McKernan et al. 2004, 2005; Cagnoni et al. 2004; Williams et al. 2005, 2006a, 2006b). However, current instrumental resolution cannot distinguish between Galactic and the Local Group origin of the absorbing gas. While a number of studies proposed these absorption lines are produced by the intragroup medium in the Local Group (see, e.g., Nicastro et al. 2002; Williams et al. 2005, 2006a, 2006b), other evidence suggests a Galactic-origin of this hot gas (Wang et al. 2005; Yao & Wang 2005; Fang et al. 2006; Yao & Wang 2007; Bregman & Lloyd-Davies 2007).

Fang et al. (2002, hereafter FANG02) reported the first

<sup>1</sup> Department of Physics and Astronomy, University of California, Irvine, CA 92697, fangt@uci.edu; *Chandra* Fellow

<sup>2</sup> Department of Physics and Center for Space Research, MIT, 77 Mass. Ave., Cambridge, MA 02139

detection of an intervening X-ray absorber at  $z = 0.0554$  along the sightline toward PKS 2155-304, using the *Chandra* LETGS. At the same redshift a small group of galaxies had been detected by Shull et al. (1998), who subsequently reported the detection of O VI (Shull et al. 2003). Subsequent observations with *XMM*-Newton did not detect the O VIII absorption, setting a  $3\sigma$  upper limit equivalent width (EW) of  $\sim 14$  mÅ compared to our reported EW of  $14.0^{+7.3}_{-5.6}$  mÅ (Cagnoni et al. 2004). Several O VII and O VIII absorption lines were detected along the sightline toward H 1821+621 (Mathur et al. 2003), although the statistics is low and the detections are at  $2 - 3\sigma$  level. McKernan et al. (2003) claimed detection of an intervening absorption system at  $z \approx 0.0147$  toward 3C 120 at  $\gtrsim 3\sigma$  level, although they cannot rule out the possibility that this system is intrinsic to the jet of 3C 120. Recently, during an extremely bright state of Mkn 421, Nicastro et al. (2005) detected two intervening absorption systems ( $z > 0$ ) with high significance. However, observations with the *XMM*-Newton cannot confirm the detections, and the consistency between the *Chandra* and *XMM*-Newton was investigated (Ravasio et al. 2005; Williams et al. 2006c; Kasstra et al. 2007; Rasmussen et al. 2007).

In this paper, we confirm detection of the intervening absorber toward PKS 2155-304 using new observations to re-examine the results from FANG02. PKS 2155-304 has been used repeatedly as a *Chandra* and *XMM*-Newton calibration target because it is one of the brightest extragalactic soft X-ray sources, and also because of its relatively simple spectrum shape. Since we published FANG02, five more *Chandra* observations with the same instrumental configuration (LETG+ACIS) were conducted, which more than triples the total exposure time that was reported in FANG02. The increase in the number of detected photons (by a factor of  $\sim 5$ ) improves the statistics of the spectrum significantly. We also analyze the *XMM*-Newton observations on the same target, as well as observations using the *Chandra* LETG+HRC combination. These observations have been used to challenge our reported detection.

## 2. DATA ANALYSIS

At  $z = 0.112$ , PKS 2155-304 ( $\alpha = 21^h 58^m 52.1^s$ ,  $\delta = -30^\circ 13' 32.1''$ ) is one of the brightest extragalactic X-ray sources. This source has been chosen to calibrate various instruments onboard *Chandra* and so is observed repeatedly. For our purpose, we choose observations that have been conducted with the Low Energy Transmission Gratings (LETG) and ACIS-S as the focal plane detector<sup>3</sup>, to be consistent with FANG02. In section §4, we will discuss results from observations using LETG with HRC-S as the focal plane detector.

In FANG02, we report the results from three observations that were conducted during May and December of 2000 and November of 2001, with a total exposure time of  $86.7$  ksec. Subsequently, seven more observations were conducted between June 2002 and September 2005. We select those observations with at least  $30$  ksec exposure time, which results in a total of five more observations. Including these five more observations increases the total exposure time to  $\sim 277$  ksec, and the number of counts in the spectral regions of interests is also increased by a factor of  $\sim 5$ . Table 1 lists the observation log. Seven of the eight observations have the nominal offset pointing for LETG+ACIS-S: the aimpoint is moved by  $\Delta y = +1.5'$  along the observatory  $y$  direction so that the most interested

TABLE 1  
OBSERVATION LOG

Observation ID	Observation Date	Duration (ksec)	Reference
1703	31 May 2000	26.7	1,2
2335	06 Dec 2000	30.0	1,2
3168	31 Nov 2001	30.0	1,2
3669	11 Jun 2002	50.0	2
3707	30 Nov 2002	30.0	2
4416	16 Dec 2003	50.0	2
6090	25 May 2005	30.0	2
6091	19 Sep 2005	30.0	2

REFERENCES. — 1. Fang et al. (2002); 2. this paper.

wavelength range ( $0 - 26$  Å) can be covered entirely by back-side chip S3, which has higher quantum efficiency and large effective area, and the Scientific Instrument Module (SIM) is moved by ( $SIM - Z = -8$  mm), to mitigate the CTI (Charge Transfer Inefficiency)-induced energy resolution degradation. This also avoids putting the zeroth-order at one of the node boundaries. The only exception is Obs.#3669, which had a  $y$ -offset of  $3.3'$ . This put the aimpoint on chip S2.

Data analysis is performed as described in FANG02. We briefly summarize here and refer the reader to that paper for more details. The *Chandra* LETGS produces a zeroth order image at the aim-point on the focal plane detector, the ACIS-S array, with higher order spectra dispersed to either side. The LETGS provides nearly constant spectral resolution ( $\Delta\lambda = 0.05$ ) through the entire bandpass (0.3-5 keV). The moderate energy resolution of the CCD detector ACIS-S is used to separate the overlapping orders of the dispersed spectrum. We add the plus and minus sides to obtain the first order spectrum. All the five data sets are analyzed with the standard *Chandra* Interactive Analysis of Observations (CIAO)<sup>4</sup> and customized Interactive Data Language (IDL) routines.

## 3. CONTINUUM SPECTRAL ANALYSIS

The continua are typically fitted with a power law modified by neutral hydrogen absorption in the range between 6 and 42 Å. For observations #1703, 2335, and 3168 we refer to FANG02 for detailed model parameters. For #3669, the data is best fitted with a broken power law. The photon indices are  $2.52 \pm 0.02$  and  $1.96 \pm 0.02$ , with a break energy of  $\sim 2$  keV, and a flux of  $1.66 \times 10^{-10}$  ergs cm $^{-2}$  s $^{-1}$  between 0.5 and 2.4 keV. The remaining four observations can be best fitted by a single power law with photon indices of  $(2.69 \pm 0.02, 2.69 \pm 0.02, 2.58 \pm 0.01, 2.66 \pm 0.01)$ , for #3707, 4416, 6090, and 6091, respectively. The flux between 0.5 and 2.4 keV is  $(5.06, 5.69, 10.33, 6.54) \times 10^{-11}$  ergs cm $^{-2}$  s $^{-1}$ , respectively. All the models include a Galactic absorption fixed at  $N_H = 1.36 \times 10^{20}$  cm $^{-2}$  (Lockman & Savage 1995; errors are quoted at 90% confidence).

In Figure 1 we show the raw counts of the five observations. The bin size is 0.025 Å. The line spread function (LSF) of LETGS has a typical full width of half maximum (FWHM) of  $\sim 0.05$ . In this way one FWHM will contain two bins. Two vertical dashed lines indicate the wavelength of the redshifted O VIII line (at  $\sim 20$  Å) reported by FANG02, and rest O VII

<sup>3</sup> For LETG and ACIS-S, see <http://asc.harvard.edu>

<sup>4</sup> See <http://asc.harvard.edu/ciao>

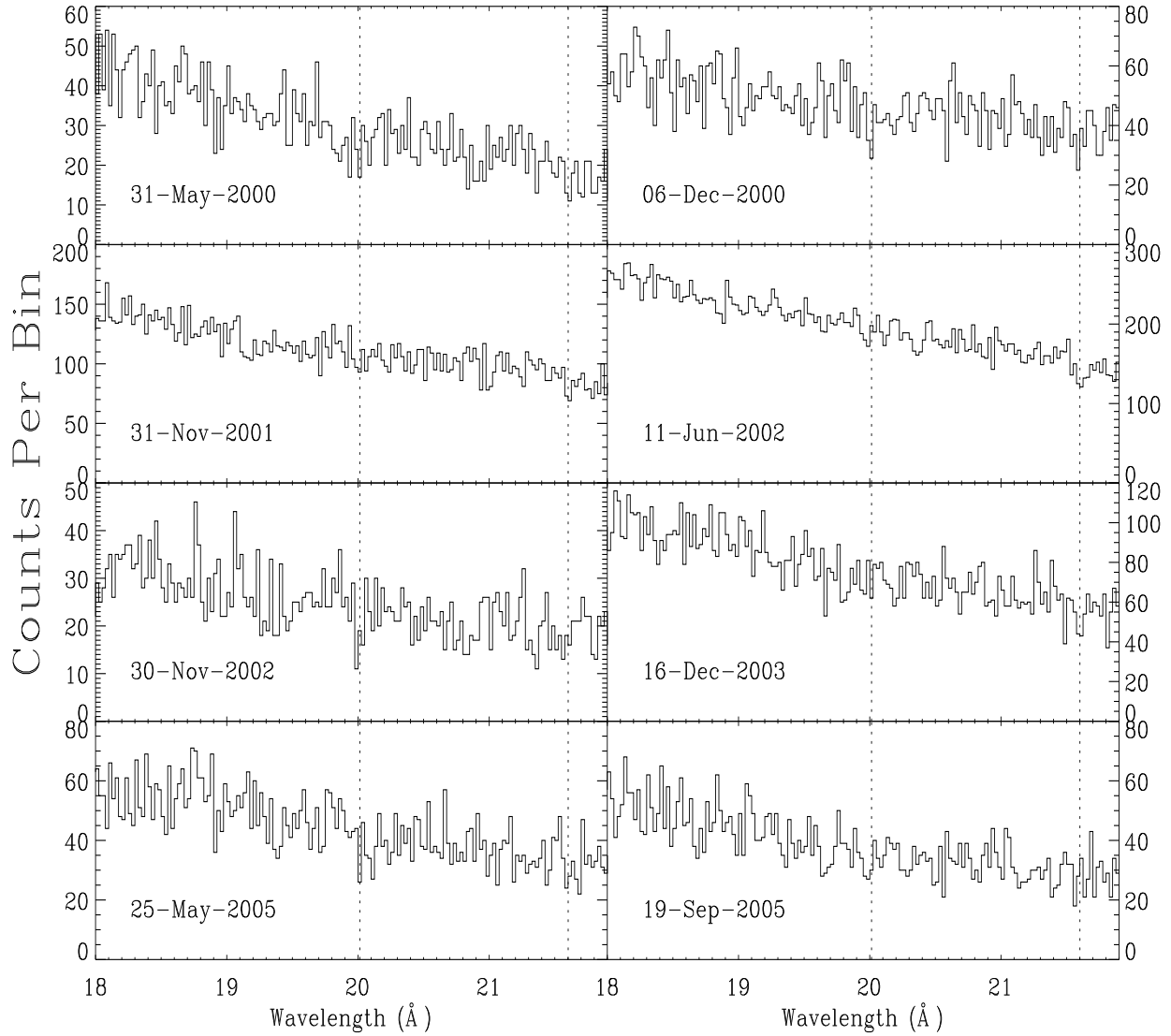


FIG. 1.— Raw counts for the five observations between 18 and 22 Å. Bin size is 0.025 Å. Two vertical dashed lines indicated positions of the redshifted O VIII and rest O VII lines from FANG02.

lines (at  $\sim 21.6$  Å). There are no strong absorption lines in these observations, but we do find small dips in each of these observations at the corresponding positions.

To enhance the signal we stack all the eight data sets. To ensure that all the eight observations are properly aligned with each other, we also compare the wavelengths of two known features, atomic O I from our Galaxy and solid-state O I from the instruments, and calibrate the five data sets against these two lines (FANG02). Only two observations (1703 and 2335) showed a systematic shift of  $\sim 0.05$  Å shift, and we have to adjust the shift manually. Figure 2 shows the stacked data between 18 and 22 Å. We have achieved from  $\sim 450$  to 600 counts per bin here, compared to  $\sim 100$  counts per bin in FANG02. We again mark the positions of the two absorption lines.

Measurement of narrow absorption features depends crucially on determining the correct continuum level. However, a simple power law cannot provide the best fit to the continuum of the stacked data for: 1) there are spectral variations among different observations, and 2) there are residual uncertainties in instrumental efficiencies. Instead we fit the local continuum

using polynomials. More specifically, we first fit the stacked data with a single power law plus neutral hydrogen absorption as an initial guess. The residuals between 6 and 42 Å are then fitted with a six-order polynomial. Such a polynomial will get rid of any features with a characteristic scale of  $\gtrsim 6$  Å, but smaller features will be preserved. Furthermore, to account for small scale fluctuations, we divide the regions between 6 and 42 Å into 9 bands, with a bandwidth of 4 Å each. For each region we then fit the residuals from the previous power law fitting with a polynomial. The order of this polynomial is given by the one that has the smallest  $\chi^2$ . The red lines in Figure 2 show the final result of the fitted continuum in the 18 – 22 Å range. The top panel shows the spectrum in units of counts per bin, with a binsize of 25 mÅ, and the bottom panel shows the flux, in units of photons  $\text{cm}^{-2}\text{s}^{-1}$ .

How well does our model depict the observed continuum? We first calculate the  $\chi$ -distribution of the data.  $\chi$  is defined as:

$$\chi = \frac{\text{data count} - \text{model count}}{(\text{model count})^{1/2}}. \quad (1)$$

We then run 10,000 Monte-Carlo simulations, each simula-

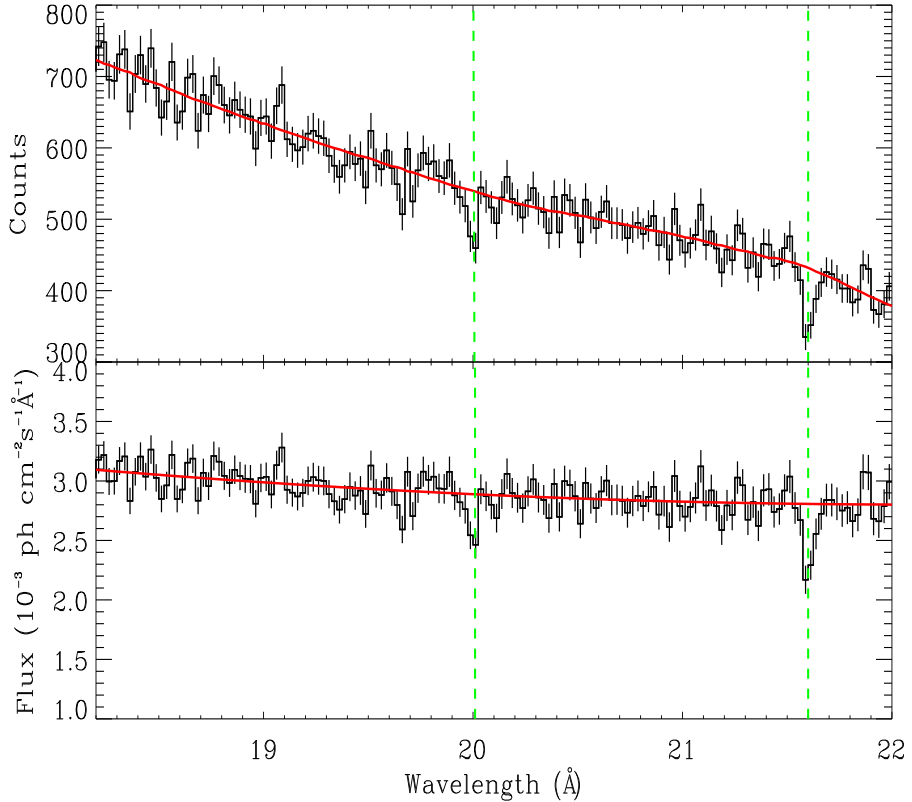


FIG. 2.— The top panel shows the raw counts of the stacked data, with a binsize of  $0.025 \text{ \AA}$ . The bottom panel shows the flux spectrum. The red line show the best fitted model. Two vertical green dashed lines indicate positions of the redshifted O VIII and rest O VII lines from FANG02.

tion is a random realization of the model based on Poisson statistics, and we also calculate the  $\chi$ -distribution of these simulations. Figure 3 shows the comparison between the data (dark line) and the simulation (red line). We find in general the  $\chi$ -distribution of the data follows that of the simulation reasonably. The data does show a long, negative tail, this is actually caused by the absorption features that we will discuss below. Excluding the three prominent absorption features that we will discuss in the next section, we perform a Kolmogorov-Smirnov test on the two distributions. The null hypothesis that the data sets are drawn from the same distribution has a significant level of  $\sim 0.48$ , suggesting that our model fits the continuum quite well, and that our fitting procedure does take care of small scale fluctuations.

#### 4. RESULTS

A blind search of the entire region from 6 to  $42 \text{ \AA}$  for features at  $> 3\sigma$  level give only three prominent absorption features, at  $\sim 20.0, 21.6$ , and  $23.5 \text{ \AA}$ . The last one is an interstellar O I line and will not be discussed here. These two features at  $20.0$  and  $21.6 \text{ \AA}$  are subsequently analyzed with customized routines from the software package ISIS (Interactive Spectral Interpretation System, see Houck & Denicola 2000)<sup>5</sup>. Specifically, we subtract the data from the best-fit model, and then fit the residual with a Gaussian line profile. The EW is an integration of  $(1 - I/I_0)$ , where  $I$  is the observed spectrum, and  $I_0$  is the continuum. We list the fitting parameters in Table 2. The Gaussian line fitting gives a line width ( $\sigma = 0.017$  and

$0.021$  for the  $20.0$  and  $21.6 \text{ \AA}$  lines, respectively) that is even narrower than that of the instrumental LSF, we only present the 90% upper limits on the intrinsic line widths. In calculating SNR (signal-to-noise ratio), signal is the total photon counts missed in the line, and noise is square-root of continuum photon counts within the line profile. The continuum photon counts are the total of counts under continuum, with a width of three times the measured line width, slightly larger than the FWHM of the fitted Gaussian line. In Figure 4 we show the residual spectra of both features (black lines) and the fitted Gaussian lines (red lines).

#### 4.1. Contamination from the Telescope Features?

Before we proceed to further discussion, we need to understand the effects of any fixed-position detector features (such as those chip gaps and node boundaries) and instrumental features (such as those absorption edges in the telescope materials). While over the entire wavelength range the telescope has been well calibrated, it is still likely that some of the variations of the effective area and/or detector quantum efficiency across these features can affect the estimated significances of our detected lines, if it happens that the detected lines are close to these telescope features.

We do not find any instrumental features near our two detected lines (POG<sup>6</sup>, Table 9.4). The positions of detector features depend on the aimpoint of each observation. For commonly used offset pointing ( $\Delta y = 1.5'$  and  $\text{SIM} - Z =$

<sup>5</sup> see <http://space.mit.edu/ASC/ISIS/>

<sup>6</sup> *Chandra Proposers' Observatory Guide*, see <http://asc.harvard.edu/propose/POG>

TABLE 2  
LINE FITTING PARAMETERS

	O VIII Ly $\alpha$ <sup>a</sup>	O VII He $\alpha$ <sup>a</sup>
Wavelength	$20.00 \pm 0.01$	$21.60 \pm 0.01$
$cz$ (km s $^{-1}$ )	$16307 \pm 158$	$-26 \pm 138$
Line Width <sup>b</sup>	$< 0.027$	$< 0.029$
Line Flux <sup>c</sup>	$2.1^{+0.6}_{-0.8}$	$3.9^{+0.8}_{-1.1}$
EW (m)	$7.42^{+2.76}_{-1.94}$	$13.75^{+4.09}_{-2.80}$
SNR <sup>d</sup>	5.0	7.1

a. Rest-frame wavelengths for O VIII Ly $\alpha$  and O VII He $\alpha$  are 18.9689 Å and 21.6019 Å respectively (Verner et al. 1996). Errors are quoted at 90% confidence level hereafter.

b. 90% upper limit of the intrinsic line width  $\sigma$ , in units of Å. The FWHM of the fitted Gaussian line is  $2.35\sigma$ .

c. Absorbed line flux in units of  $10^{-5}$  photons cm $^{-2}$ s $^{-1}$ .

d. In units of equivalent sigma of a Gaussian distribution with the same confidence level as the Poisson significance gives, based on the  $\chi$ -distribution.

–8mm), the nominal aimpoint in S3 chip is moved from (chipx, chipy)=(231, 502) to (chipx, chipy)=(49, 168), which also avoids the zeroth-order being at one of the node boundaries. A careful calculation indicates no telescope features around the 21.6 Å line, but such configuration does put the positive first order 20.0 Å line close to the boundary between node 2 and node 3 in S3 chip. However, we believe this is unlikely to have large impact on the significance of the 20.0 Å line because of the following considerations. First, as we stated before, Obs.#3669, the one with the most photon counts (accounts for almost half of the total counts at 20.0 Å), had a y-offset of 3.3', which put the aimpoint in chip S2. This results in the positive first order 20.0 Å line being far away from any telescope features. Secondly, this line is clearly visible in both positive and negative first order spectra. It is unlikely that this line would be detected in the negative order if it is caused by detector feature in the positive order. Thirdly, and most importantly, we believe that our continuum-extraction technique can take care of the small variation caused by node boundaries. During most observations, the spacecraft is dithering to (1) smear out the reduced exposure from chip gaps, and (2) smooth out pixel-to-pixel variation in the response (see POG). The standard dithering pattern has a peak-to-peak width of 16'', this roughly corresponds to a response variation on the scale of  $\sim 1$  for LETGS. However, based on the fitting procedures we described in section §3, the residual between 18 and 22 Å, after broadband continuum-fitting with a power law and 6-order polynomial, was fitted with another 6-order polynomial. This would get rid of any feature with a typical scale of  $\gtrsim 0.7$ , which includes the dithered node boundary.

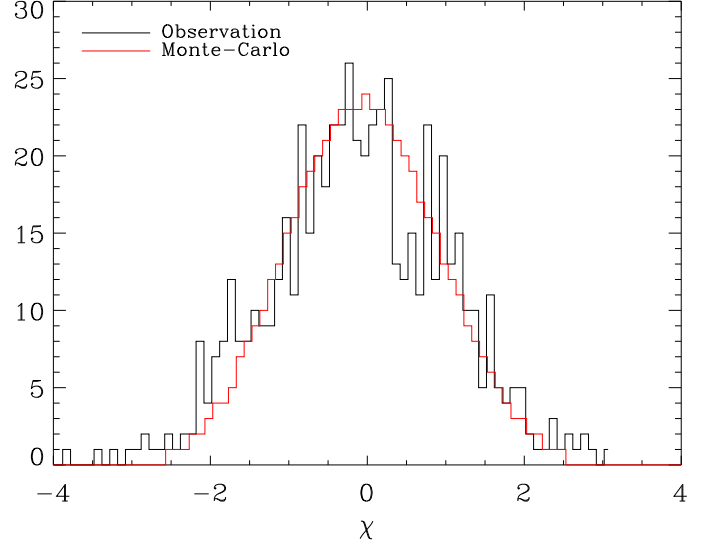


FIG. 3.—  $\chi$ -distribution of the data (dark line) and of 10,000 Monte-Carlo simulations (red line).

The effect of such procedure can be viewed from Figure 2: in the top panel, the raw counts spectrum shows some variation between 19 and 21 Å, however, in the bottom panel, such variation has been smoothed out in the flux spectrum.

#### 4.2. Comparison with results from FANG02

Most importantly, our work does detect an absorption line at  $5\sigma$  significance at  $\sim 20$  Å, confirming the initial detection by FANG02. We find that the results presented in this paper are consistent with those of FANG02, but the estimated EW in this work ( $7.42^{+2.76}_{-1.94}$ ) is about one-half of that estimated earlier, based on many fewer counts (150 vs. 550 counts per bin) and with larger uncertainty. The two results are consistent at 90% confidence level. The properties of the stronger local ( $z \approx 0$ ) O VII absorption line are fully consistent with those reported in FANG02.

#### 4.3. Comparison with results from Chandra LETG+HRC-S

For a consistency check, we also analyzed the observations up to a date of 2004 November 22 taken with the LETG operated with High Resolution Camera for spectroscopy (HRC-S; Table 3). We reprocessed these observations using the *Chandra* Interactive Analysis of Observations (CIAO) software (ver. 3.3.0.1) with the calibration database CALDB (ver. 3.2.1). Because the HRC itself does not have intrinsic energy resolution, the photons located to the same position of the grating arms but from different grating orders cannot be sorted out as in those observations with ACIS. We therefore used a forward approach to account for the spectral order overlapping. For each observation, we first calculated the response matrix files (RMFs) and the auxiliary response functions (ARFs) for grating orders from the first to sixth (assuming the contributions to the spectrum from the higher  $> 6$  orders are negligible). We then added these six RMF and ARF pairs to form an order-combined response (RSP) file using IDL routines from PINTofALE package<sup>7</sup>. To enhance the counting statistics, spectra from all the HRC-S observations, after a consistency check, were co-added, and the RSP

<sup>7</sup> <http://hea-www.harvard.edu/PINTofALE>

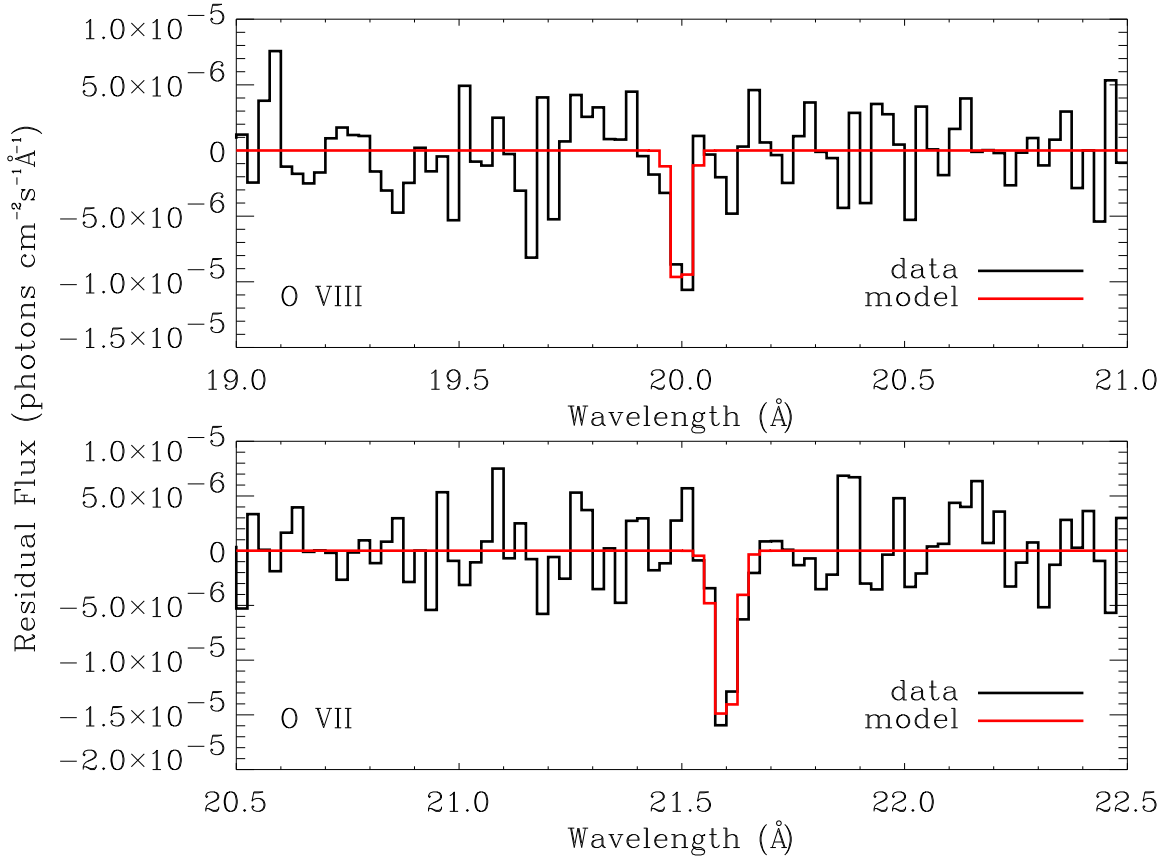


FIG. 4.— Residual flux after subtracting the best-fitted continuum from the stacked data. The red lines show the ISIS-fitted Gaussian line profiles. The top panel is for the redshifted O VIII line and the bottom panel is for the zero-redshift O VII line.

TABLE 3  
HRC OBSERVATIONS

ObsID	Date	Exposure (ks)
331	1999 Dec. 25	63.2
1013	2001 Apr. 06	26.8
1704	2000 May 31	26.0
3166	2001 Nov. 30	30.0
3709	2002 Nov. 30	13.8
4406	2002 Nov. 30	13.9
5172	2004 Nov. 22	27.2

files are weight-averaged based on the corresponding exposure time and the continuum intensity obtained from a global fit to each individual spectrum.

In Fig. 5 we show the total HRC spectrum (from the first to sixth order) between 18 and 22 Å. The 21.6 Å line is clearly visible, but not the 20.0 Å line. There are some hints of absorption features between 19 and 20 Å, but nothing near the LETG+ACIS detected 20.0 Å line. We cannot extract the first order spectrum because of the reason we described above, but using a first order response matrix, we estimate the continuum flux of the first order is about 90% of the total flux, which gives  $\sim 450$  counts per 0.025 Å at  $\sim 20.0$  Å region. The observations with the LETG+ACIS have a slightly stronger continuum ( $\sim 550$  counts per 0.025 Å at the same

wavelength). We estimate the upper limit of an absorption line EW, by adding such line in the spectrum and calculating  $\Delta\chi^2$  by varying line EW. This gives an upper limit of  $\sim 9$  mÅ, which is consistent with the result from the LETG+ACIS observations.

To further investigate the difference between the results from the LETG+ACIS and LETG+HRC, we compare their LSFs. In Figure 6, we show the LSFs of the LETG+ACIS (red line) and the LETG+HRC (green line) at 20 Å. The blue line is the LSF of the XMM RGS1, and we will discuss it later. Clearly, the HRC curve has a rather broad wing. This suggests that when compared with that of the ACIS, more photons will be distributed in the wing, and the significance at the line center will be lower. Such broader profile is likely caused by the non-linearities of the LETG+HRC-S dispersion relation<sup>8</sup>. To test the impact of the LSF, we run 10,000 Monte-Carlo simulations for both the LETG+ACIS and the LETG+HRC, based on the Poisson statistics. Each simulation is a random realization of the corresponded continuum model plus an absorption line at 20 Å. We adopt line parameters from the O VIII line in Table 2 with an intrinsic line width of 0.016 Å, and then fold it through the corresponded LSF. We find that out of 10,000 trials, the line is detected at  $3\sigma$  level or higher in more than half of the ACIS simulated spectra ( $\sim 57\%$ ); however, for the HRC spectra, the detection probability decreases to about one-fourth ( $\sim 25\%$ ).

<sup>8</sup> For detailed discussion on the non-linearities of the LETG+HRC-S dispersion relation, see <http://cxc.harvard.edu/cal/Letg/Corrlam/>.

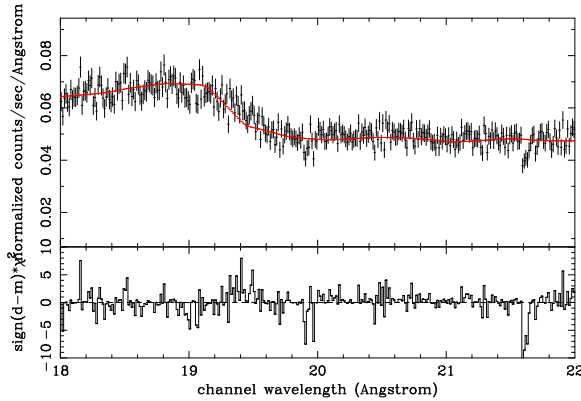


FIG. 5.— LETG+HRC spectrum. The red line in the top panel is the model. The bottom panel shows  $\chi^2$  with a sign.

#### 4.4. Comparison with results from XMM-Newton

PKS 2155-304 was also extensively observed with XMM-Newton. A detailed spectroscopy study of the RGS data was presented by Cagnoni et al. (2004). They confirm the detection of zero-redshift O VII absorption line at a significance level of  $4.5\sigma$ . Their best fit equivalent width ( $EW = 19.50^{+7.89}_{-8.17}$  mÅ) is higher than what we measure but consistent at 90% confidence level. They also claim that this line profile is possibly double peaked. Although the *Chandra* LETG+ACIS has higher energy resolving power, we cannot confirm this structure in our data.

Cagnoni et al. (2004) stated that they do not detect the redshifted O VIII absorption line at  $\sim 20$  Å, reported by FANG02, and set a  $3\sigma$  upper limit of 14 mÅ. However, this value is large enough to be consistent with both the improved measurement and the original best fit value of FANG02 for the detected line.

To further compare the *Chandra* and XMM-Newton data, we reanalyze the XMM-Newton data presented in Cagnoni et al. (2004) with the same techniques adopted in this paper. In doing this we hope we can minimize the differences that can be caused by various data analysis techniques. For instance, whereas we apply a adapted-polynomial plus power law fit technique to subtract continuum, they use local absorbed power law to fit individual regions with bandwidths of 2–3 Å.

We use the three data sets that were analyzed in Cagnoni et al. (2004) (ObsID #0080940101, 0080940301, and 0080940401). We do not select the fourth observation (ObsID #0080940501) because it contains a background flare. These three observations have a total exposure time of  $\sim 110$  ksec (see Table 1 of Cagnoni et al. (2004) for detailed observation log). We analyze the data with the standard Science Analysis System (SAS) version 5.4.1<sup>9</sup>. We use only RGS-1 data since there is no data between 20 and 24 Å from RGS-2 due to the failure of a CCD chip. The LSF of the RGS-1 has a FWHM of  $\sim 0.06$  Å with rather extended wings<sup>10</sup>. We will not present our data extraction procedures here, but refer reader to Cagnoni et al. (2004) for details. After obtaining the first order spectrum, we follow procedures that are described in section §3 to subtract the continuum. Figure 7 shows the RGS-1 spectrum between 19.7 and 20.7 Å. We obtain  $\sim 450$  counts per 0.025 Å bin. This is 20% lower than what we ob-

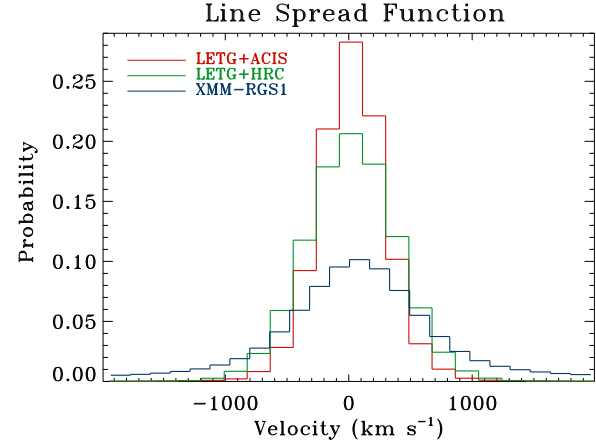


FIG. 6.— The line spread functions of the *Chandra* LETG+ACIS (red), the *Chandra* LETG+HRC (green), and the XMM RGS1(blue) at 20 Å.

served in *Chandra* data ( $\sim 550$  counts per 0.025 Å).

The dark solid line in figure 7 shows the XMM data between 19.5 and 20.5 Å. No absorption line is seen around  $\sim 20$  Å. With our continuum subtraction techniques, we obtain a  $3\sigma$  upper limit of  $\sim 10$  mÅ, consistent with what is obtained in Cagnoni et al. (2004) and the  $\sim 7$  mÅ equivalent width line we report in this paper. To demonstrate this, in Figure 7 we plot a  $3\sigma$ , 10 mÅ line at  $\sim 20$  Å in green. An illustration (but without imposing statistical fluctuations) of how the line detected in *Chandra* would appear in the XMM data is plotted in red. We adopt our *Chandra* line parameters, and then convolve the line with the RGS1 LSF<sup>11</sup>.

In Figure 8 we show the  $\Delta\chi^2$  of fitting the XMM data with a continuum plus a Gaussian line model (again, convolved by the LSF), where  $\Delta\chi^2 = 0$  is defined as no Gaussian line. We fix the line center at  $\lambda = 20$  Å, and gradually vary the line equivalent width. The horizontal dashed line indicates the  $\Delta\chi^2 = 9$ , or  $3\sigma$  confidence. Three vertical dark lines show the line width and 90% lower and upper limits of our detection. Again, we find that one would not have expected XMM-Newton to detect the line seen with *Chandra*.

Two main reasons that explain the non-detection of the X-ray absorption line in the *Chandra* LETG+HRC data may also apply there. First, the continuum is slightly higher in *Chandra* data. At 20 Å, the *Chandra* observations show  $\sim 550$  counts per bin, compared with  $\sim 450$  counts in the XMM data. Secondly, and most importantly, the LSF of the RGS1 not only is larger than that of the LETGS, but also has rather extended wings. As pointed out by Williams et al. (2006) in a study of the XMM data of Mrk 421, the central 0.1 Å region of a line contains about 96% of the total line flux for *Chandra* LETG, for RGS this number decreases to  $\sim 68\%$ . In Figure 6 the dotted line is the LSF of the RGS1. The wings of the RGS1 are even broader than that of the LETG+HRC. We ran a similar Monte-Carlo simulation on the RGS1 data. The result supports our finding: out of 10,000 trials, a  $3\sigma$  line is detected in only  $\sim 10\%$  RGS1 spectra, compared with nearly  $\sim 57\%$  detection in the LETG+ACIS spectra, and  $\sim 25\%$  detection in the LETG+HRC spectra.

## 5. DISCUSSION

<sup>9</sup> See <http://xmm.vilspa.esa.es/>

<sup>10</sup> See XMM-Newton Users' Handbook at <http://xmm.vilspa.esa.es/>.

<sup>11</sup> A template of the LSF was kindly provided by A. Rasmussen.

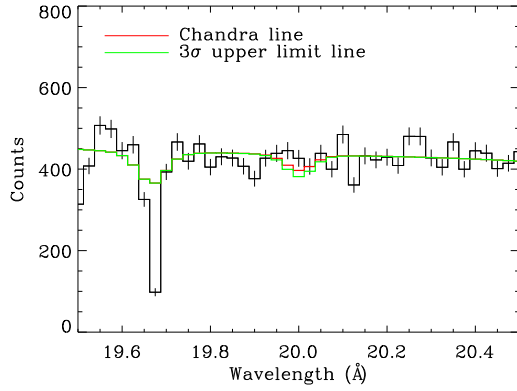


FIG. 7.— XMM data at  $\sim 20$  Å. The dark line shows the data, the green line shows the continuum with a  $3\sigma$  absorption line, and the red line shows the continuum with the line detected in *Chandra* data. The line at  $\sim 19.75$  Å is an instrumental feature.

Following FANG02 and assuming that the line is not saturated, the column density of the redshifted O VIII absorption line at 20 Å is  $N(\text{O VIII}) = 5.0_{-1.3}^{+1.9} \times 10^{15} \text{ cm}^{-2}$ . The line width sets an upper limit to the path length of  $\sim 5.8 h_{70}^{-1} \text{ Mpc}$  based on the Hubble flow<sup>12</sup>. This gives  $n_b > 5 \times 10^{-6} \text{ cm}^{-3} Z_{0.1}^{-1} f_{0.5}^{-1} l_{5.8}^{-1}$  where  $Z_{0.1}$  is the metallicity in units of 0.1 solar abundance<sup>13</sup>,  $f_{0.5}$  is the ionization fraction in units of 0.5 and  $l_{5.8}$  is the path length in units of  $5.8 h_{70}^{-1} \text{ Mpc}$ . A lower limit to the path length of  $\sim 1$  Mpc can be obtained by assuming the absorber has the size of the small galaxy group detected in 21 cm images (Shull et al. 1998), which gives  $n_b \approx 3.1 \times 10^{-5} \text{ cm}^{-3} Z_{0.1}^{-1} f_{0.5}^{-1}$ . This implies a range of baryon overdensities of  $\delta_b \approx 30-150$ , which, as found in FANG02, is consistent with the predicted density of the WHIM gas from cosmological hydrodynamic simulations (see, e.g., Cen & Ostriker 1999; Davé et al. 2001).

To constrain the temperature we need to study the ionization structure of the O VIII absorber. Assuming collisional ionization equilibrium, the ionization fraction is a function of temperature only, and  $f(\text{O VIII})$ , the ionization fraction of O VIII, has a peak value of  $\sim 0.5$  between 2 and  $5 \times 10^6$  K. A constraint on the temperature of the O VIII absorber can be obtained by studying the column density ratio between O VIII and O VII. Non-detection of the O VII at the corresponding redshifted position ( $\lambda = 22.77$  Å) with a  $3\sigma$  upper limit on the equivalent width of  $\sim 9.6$  mÅ, implies  $N(\text{O VII}) \lesssim 3 \times 10^{15} \text{ cm}^{-2}$ , or  $\log[N(\text{O VIII})/N(\text{O VII})] \gtrsim 0.22$ . This constrains the temperature to be  $T \gtrsim 2.3 \times 10^6$  K. However, we need to be careful about the assumption of collisional ionization equilibrium (Cen & Fang 2006).

We can actually strengthen the constraint on temperature by searching for potentially co-existing absorption lines at other wavelengths. Recently, Shull et al. (2003) reported the detection of a series of H I and O VI absorbers along the sight line towards PKS 2155-304 between 16185 and 17116 km s<sup>-1</sup>. Based on FANG02 they resorted to a multi-phase model to

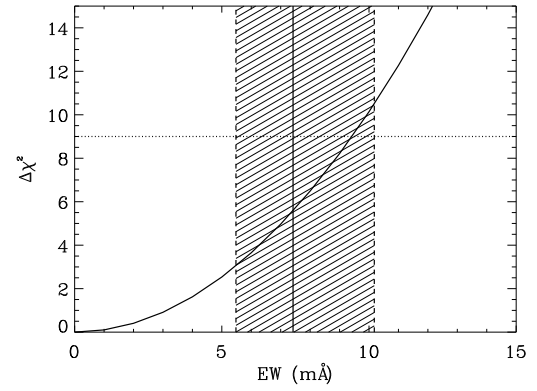


FIG. 8.—  $\Delta\chi^2$  from fitting XMM data with a continuum plus a Gaussian line. The horizontal line shows the  $3\sigma$  upper limit. The shaded red area indicates the equivalent width and 90% confidence range of the line that is detected in *Chandra* data.

explain the kinematic offsets among H I, O VI and O VIII absorbers. The new measurement presented here indicates that these absorbers may coexist owing to the small separation in velocity space. For instance, the X-ray absorber may coexist with the component A in their observation, which is located between 16185 and 16252 km s<sup>-1</sup> and shows O VI absorption line. If this is indeed a single absorber, we can set a tight range of the O VI-to-O VIII ratio:  $-2.68 \lesssim \log[N(\text{O VI})/N(\text{O VIII})] \lesssim -1.90$ . This in turn sets temperature:  $1.6 \lesssim T \lesssim 2.3 \times 10^6$  K. Using the previous constraint from the O VIII-to-O VII ratio, we can put a tight constraint on the temperature of the component A:  $T \approx 2.3 \times 10^6$  K.

Our discussion on the density and temperature of the 20.0 Å absorber depends on several crucial assumptions that need to be closely examined. First, we assume the line is unsaturated. However, the 90% upper limit on the intrinsic line width can only give a Doppler- $b$  parameter of  $\lesssim 566$  km s<sup>-1</sup>, much larger than the typical thermal broadening width  $\sim 50$  km s<sup>-1</sup> of a few million-degree gas. The non-detection of the high-order Lyman series, particularly the Ly $\beta$  line at the rest-frame of  $\sim 16$  Å, can rule out the saturate scenario at  $1\sigma$  level only, and we notice in some cases the local X-ray absorption line could be saturated (Williams et al. 2006; Yao & Wang 2006, 2007). If the line is saturated, the derived column density can be treated as a lower limit only. If the line is indeed unsaturated, it will be broad. As suggested by the clump-infall model in Shull et al. (2003), a shock-wave of  $\sim 400$  km s<sup>-1</sup> from structure evolution can provide such a non-thermal broadening mechanism: such a shock-wave would produce a post-shock temperature of  $\sim 2 \times 10^6$  K.

Secondly, we assume the gas is in collisional ionization equilibrium. Recent study, using numerical simulation, shows that non-equilibrium evolution of various ion species can produce significantly different effects (Cen & Fang 2006; Yoshikawa & Sasaki 2006), since the timescales for ionization and recombination are not widely separated from the Hubble timescale. Also, the relaxation process between electrons and ions may produce a two-temperature structure in the IGM and have impact on the metal ionization fraction, since the relaxation time is comparable to the Hubble timescale (Yoshida et

<sup>12</sup> We use  $H_0 = 70 h_{70} \text{ km s}^{-1} \text{ Mpc}^{-1}$ , and a standard  $\Lambda$ CDM model with  $\Omega_m = 0.3$  and  $\Omega_\Lambda = 0.7$  throughout the paper

<sup>13</sup> We adopt solar abundance from Anders & Grevesse (1989)

al. 2005). However, we expect such process would be more important for hotter gas at  $T > 10^7$  K (Yoshida et al. 2005). At very low density, especially at  $n_b \lesssim 10^{-5}$  cm $^{-3}$ , photoionization can also become important (see, e.g., Hellsten et al. 1998; Nicastro et al. 2002; Chen et al. 2003; Williams et al. 2005). For instance, at  $n_b = 10^{-6}$  cm $^{-3}$ , the O VIII ionization curve peaks at  $\sim 3 \times 10^5$  K under the cosmic X-ray background radiation (Chen et al. 2003).

Finally, we discuss the coexistence of O VI and O VIII absorbers primarily because of the proximity in radial velocities. However, as suggested by Shull et al. (2003), the O VI line width is narrow ( $40 \pm 10$  km s $^{-1}$  FWHM), and the scenario that O VI and O VIII can coexist is marginally plausible within measurement errors ( $\log T \approx 6.25 \pm 0.1$ ).

The baryonic content  $\Omega_b$ (O VIII) that is probed by the O VIII absorption can be estimated following Lanzetta et al. (1995) and Tripp et al. (2000). Given the path length of the sight line toward PKS 2155-304 of  $\Delta z \approx 0.116$  and assuming an upper limit of metallicity of  $0.5Z_\odot$ , we estimate  $\Omega_b$ (O VIII)  $\gtrsim 0.004 h_{70}^{-1}$ , or about 10% of the total baryon fraction. This number is consistent with the prediction of the WHIM gas from numerical simulations. Based on this single detection, the observed distribution  $dn/dz$ , defined as number of absorbers per unit redshift, is higher than what simulation predicts (see, e.g., Cen & Fang 2006, Fig. 4). We certainly need more detections to improve statistics.

Note: After we submitted this paper, Williams et al. (2006b)

published a paper on the *Chandra* archival data of PKS 2155-304. While they mainly focused on the local  $z = 0$  absorption lines, they also discussed the intervening absorption line we reported in FANG02. They confirmed the detection of this line using the *Chandra* LETG-ACIS. The measured equivalent width is  $(7.5 \pm 2.1$  mÅ) is consistent with what we found, although the significance is lower ( $3.5\sigma$ ). They did not detect this line using the *Chandra* LETG-HRC, but obtained an upper limit of  $\sim 12.5$  mÅ. This is in agreement with what we found with the HRC data, and is consistent with the detection in the ACIS data.

We thank Herman Marshall for providing helpful IDL tools for data analysis. We also thank the referee Fabrizio Nicastro for useful suggestions. We thank David Buote and Andrew Rasmussen for useful discussions. TF was supported by the NASA through *Chandra* Postdoctoral Fellowship Award Number PF3-40030 issued by the *Chandra* X-ray Observatory Center, which is operated by the Smithsonian Astrophysical Observatory for and on behalf of the NASA under contract NAS 8-39073. CRC and YY are supported by NASA through the Smithsonian Astrophysical Observatory (SAO) contract SV3-73016 to MIT for support of the *Chandra* X-Ray Center, which is operated by the SAO for and on behalf of NASA under contract NAS 08-03060. YY is also supported by AR7-8014.

## REFERENCES

Anders, E., & Grevesse, N. 1989, *Geochim. Cosmochim. Acta*, 53, 197  
 Bahcall, J. N., Jannuzzi, B. T., Schneider, D. P., Hartig, G. F., Bohlin, R., & Junkkarinen, V. 1991, *ApJ*, 377, L5  
 Bregman, J. N., & Lloyd-Davies, E. J. 2007, ArXiv e-prints, 707, arXiv:0707.1699  
 Cagnoni, I., Nicastro, F., Maraschi, L., Treves, A., & Tavecchio, F. 2004, *ApJ*, 603, 449  
 Cen, R., & Fang, T. 2006, *ApJ*, 650, 573  
 Cen, R., & Ostriker, J. P. 2006, *ApJ*, 650, 560  
 Cen, R., & Ostriker, J. P. 1999, *ApJ*, 514, 1  
 Chen, X., Weinberg, D. H., Katz, N., & Davé, R. 2003, *ApJ*, 594, 42  
 Croft, R. A. C., Di Matteo, T., Davé, R., Hernquist, L., Katz, N., Fardal, M. A., & Weinberg, D. H. 2001, *ApJ*, 557, 67  
 Danforth, C. W., & Shull, J. M. 2005, *ApJ*, 624, 555  
 Davé, R., et al. 2001, *ApJ*, 552, 473  
 Fang, T., Croft, R. A. C., Sanders, W. T., Houck, J., Davé, R., Katz, N., Weinberg, D. H., & Hernquist, L. 2005, *ApJ*, 623, 612  
 Fang, T., Marshall, H. L., Lee, J. C., Davis, D. S., & Canizares, C. R. 2002, *ApJ*, 572, L127  
 Fang, T., McKee, C. F., Canizares, C. R., & Wolfire, M. 2006, *ApJ*, 644, 174  
 Fang, T., Sembach, K. R., & Canizares, C. R. 2003, *ApJ*, 586, L49  
 Finoguenov, A., Briel, U. G., & Henry, J. P. 2003, *A&A*, 410, 777  
 Fujimoto, R., et al. 2004, *PASJ*, 56, L29  
 Furlanetto, S. R., Phillips, L. A., & Kamionkowski, M. 2005, *MNRAS*, 359, 295  
 Furlanetto, S. R., Schaye, J., Springel, V., & Hernquist, L. 2004, *ApJ*, 606, 221  
 Hellsten, U., Gnedin, N. Y., & Miralda-Escudé, J. 1998, *ApJ*, 509, 56  
 Houck, J. C., & Denicola, L. A. 2000, *Astronomical Data Analysis Software and Systems IX*, 216, 591  
 Kaastra, J. S., Werner, N., Herder, J. W. A. d., Paerels, F. B. S., de Plaa, J., Rasmussen, A. P., & de Vries, C. P. 2006, *ApJ*, 652, 189  
 Kaastra, J. S. 2004, *Journal of Korean Astronomical Society*, 37, 375  
 Kaspi, S., et al. 2002, *ApJ*, 574, 643  
 Kawahara, H., Yoshikawa, K., Sasaki, S., Suto, Y., Kawai, N., Mitsuda, K., Ohashi, T., & Yamasaki, N. Y. 2006, *PASJ*, 58, 657  
 Kravtsov, A. V., Klypin, A., & Hoffman, Y. 2002, *ApJ*, 571, 563  
 Kuntz, K. D., Snowden, S. L., & Mushotzky, R. F. 2001, *ApJ*, 548, L119  
 Lanzetta, K. M., Wolfe, A. M., & Turnshek, D. A. 1995, *ApJ*, 440, 435  
 Lehner, N., Savage, B. D., Richter, P., Sembach, K. R., Tripp, T. M., & Wakker, B. P. 2007, *ApJ*, 658, 680  
 Lockman, F. J., & Savage, B. D. 1995, *ApJS*, 97, 1  
 Mannucci, F., Bonnoli, G., Zappacosta, L., Maiolino, R., & Pedani, M. 2007, *A&A*, 468, 807  
 Mathur, S., Weinberg, D. H., & Chen, X. 2003, *ApJ*, 582, 82  
 McKernan, B., Yaqoob, T., & Reynolds, C. S. 2005, *MNRAS*, 361, 1337  
 McKernan, B., Yaqoob, T., Mushotzky, R., George, I. M., & Turner, T. J. 2003, *ApJ*, 598, L83  
 McKernan, B., Yaqoob, T., & Reynolds, C. S. 2004, *ApJ*, 617, 232  
 Mittal, J., Lieu, R., Cen, R., & Bonamente, M. 2004, *ApJ*, 617, 860  
 Morris, S. L., Weymann, R. J., Savage, B. D., & Gilliland, R. L. 1991, *ApJ*, 377, L21  
 Nicastro, F., et al. 2005, *Nature*, 433, 495  
 Nicastro, F., et al. 2002, *ApJ*, 573, 157  
 Oegerle, W. R., et al. 2000, *ApJ*, 538, L23  
 Penton, S. V., Stocke, J. T., & Shull, J. M. 2004, *ApJS*, 152, 29  
 Penton, S. V., Stocke, J. T., & Shull, J. M. 2000, *ApJS*, 130, 121  
 Perna, R., & Loeb, A. 1998, *ApJ*, 503, L135  
 Phillips, L. A., Ostriker, J. P., & Cen, R. 2001, *ApJ*, 554, L9  
 Rasmussen, A., Kahn, S. M., & Paerels, F. 2003, *The IGM/Galaxy Connection. The Distribution of Baryons at z=0*, 281, 109  
 Rasmussen, A. P., Kahn, S. M., Paerels, F., Herder, J. W. d., Kaastra, J., & de Vries, C. 2007, *ApJ*, 656, 129  
 Ravasio, M., Tagliaferri, G., Pollock, A. M. T., Ghisellini, G., & Tavecchio, F. 2005, *A&A*, 438, 481  
 Richter, P., Fang, T., & Bryan, G. L. 2006, *A&A*, 451, 767  
 Richter, P., Savage, B. D., Tripp, T. M., & Sembach, K. R. 2004, *ApJS*, 153, 165  
 Savage, B. D., Sembach, K. R., Tripp, T. M., & Richter, P. 2002, *ApJ*, 564, 631  
 Savage, B. D., Tripp, T. M., & Lu, L. 1998, *AJ*, 115, 436  
 Sembach, K. R., Howk, J. C., Savage, B. D., Shull, J. M., & Oegerle, W. R. 2001, *ApJ*, 561, 573  
 Sembach, K. R., Tripp, T. M., Savage, B. D., & Richter, P. 2004, *ApJS*, 155, 351  
 Shull, J. M., Penton, S. V., Stocke, J. T., Giroux, M. L., van Gorkom, J. H., Lee, Y. H., & Carilli, C. 1998, *AJ*, 116, 2094  
 Shull, J. M., Stocke, J. T., & Penton, S. 1996, *AJ*, 111, 72  
 Shull, J. M., Tumlinson, J., & Giroux, M. L. 2003, *ApJ*, 594, L107  
 Soltan, A. M., Freyberg, M. J., & Hasinger, G. 2005, *A&A*, 436, 67  
 Stocke, J. T., Penton, S. V., Danforth, C. W., Shull, J. M., Tumlinson, J., & McLin, K. M. 2006, *ApJ*, 641, 217  
 Stocke, J. T., Shull, J. M., Penton, S., Donahue, M., & Carilli, C. 1995, *ApJ*, 451, 24

Takei, Y., Henry, J. P., Finoguenov, A., Mitsuda, K., Tamura, T., Fujimoto, R., & Briel, U. G. 2007, *ApJ*, 655, 831

Takei, Y., et al. 2007, *PASJ*, 59, 339

Tripp, T. M., & Savage, B. D. 2000, *ApJ*, 542, 42

Tripp, T. M., Savage, B. D., & Jenkins, E. B. 2000, *ApJ*, 534, L1

Tumlinson, J., & Fang, T. 2005, *ApJ*, 623, L97

Tumlinson, J., Shull, J. M., Giroux, M. L., & Stocke, J. T. 2005, *ApJ*, 620, 95

Ursino, E., & Galeazzi, M. 2006, *ApJ*, 652, 1085

Verner, D. A., Verner, E. M., & Ferland, G. J. 1996, *Atomic Data and Nuclear Data Tables*, 64, 1

Viel, M., Branchini, E., Cen, R., Matarrese, S., Mazzotta, P., & Ostriker, J. P. 2003, *MNRAS*, 341, 792

Wang, Q. D., et al. 2005, *ApJ*, 635, 386

Williams, R. J., Mathur, S., & Nicastro, F. 2006, *ApJ*, 645, 179

Williams, R. J., Mathur, S., Nicastro, F., & Elvis, M. 2006, ArXiv Astrophysics e-prints, arXiv:astro-ph/0611583

Williams, R. J., Mathur, S., Nicastro, F., & Elvis, M. 2006, *ApJ*, 642, L95

Williams, R. J., et al. 2005, *ApJ*, 631, 856

Williger, G. M., Heap, S. R., Weymann, R. J., Davé, R., Ellingson, E., Carswell, R. F., Tripp, T. M., & Jenkins, E. B. 2006, *ApJ*, 636, 631

Yao, Y., Schulz, N., Wang, Q. D., & Nowak, M. 2006, *ApJ*, 653, L121

Yao, Y., & Wang, Q. D. 2005, *ApJ*, 624, 751

Yao, Y., & Wang, Q. D. 2007, *ApJ*, 658, 1088

Yoshida, N., Furlanetto, S. R., & Hernquist, L. 2005, *ApJ*, 618, L91

Yoshikawa, K., et al. 2004, *PASJ*, 56, 939

Yoshikawa, K., & Sasaki, S. 2006, *PASJ*, 58, 641

Yoshikawa, K., Yamasaki, N. Y., Suto, Y., Ohashi, T., Mitsuda, K., Tawara, Y., & Furuzawa, A. 2003, *PASJ*, 55, 879

Zappacosta, L., Maiolino, R., Mannucci, F., Gilli, R., & Schuecker, P. 2005, *MNRAS*, 357, 929

Zappacosta, L., Mannucci, F., Maiolino, R., Gilli, R., Ferrara, A., Finoguenov, A., Nagar, N. M., & Axon, D. J. 2002, *A&A*, 394, 7